Pergamon

Geochimica et Cosmochimica Acta, Vol. 65, No. 3, pp. 369–379, 2001

0016-7037/01 $20.00 + .00

PII S0016-7037(00)00531-7

Microscopic effects of carbonate, manganese, and strontium ions on calcite dissolution

A. S. LEA,* J. E. AMONETTE, D. R. BAER, Y. LIANG, and N. G. COLTON

Environmental Molecular Sciences Laboratory, Pacific Northwest National Laboratory, Box 999, MS K8-93, Richland, WA 99352, USA

(*Received September* 8, 1999; *accepted in revised form August* 23, 2000)

Abstract—Aqueous dissolution of the $(10\bar{1}4)$ surface of calcite was observed at pH near 9 by using an atomic force microscope equipped with a fluid cell. The influences of carbonate (CO_3^{2-}), strontium (Sr^{2+}), and manganese (Mn^{2+}) ion concentrations on the rates of step motion were measured. Carbonate ions were shown to have a step-specific effect on calcite dissolution. At low levels (<1 μ**M**) of CO_3^{2-}, the retreat rate of the more structurally open $[\bar{4}41]_+$ steps was faster than the retreat rate of the structurally confined $[\bar{4}41]_-$ steps, leading to anisotropic dissolution. Increasing the CO_3^{2-} level to as high as 900 μ**M** decreased the rate of retreat of both steps, but the $[\bar{4}41]_+$ step was slowed to a much greater extent changing the degree of dissolution anisotropy. This decrease in step velocity at high CO_3^{2-} levels was attributed to a corresponding increase in the back reaction (i.e., precipitation) as the solution approached saturation with respect to calcite. Strontium cations were also shown to have a step-specific effect on calcite dissolution similar to that of CO_3^{2-}. Manganese cations, on the other hand, slowed the rate of retreat of the $[\bar{4}41]_-$ step to a greater extent than Sr^{2+}. The influence of impurity metal sorption on dissolution is examined in terms of sorption at kinks and the dissolution behavior is explained in terms of a terrace-ledge-kink site-blocking model. Evidence is given to support the hypothesis that ion-pairs formed in solution are the primary growth units for calcite. *Copyright © 2001 Elsevier Science Ltd*

1. INTRODUCTION

Mineral interactions with impurities have significant environmental and geochemical implications. Partitioning between aqueous and mineral phases or incorporation into minerals can affect the fate and transport of aqueous subsurface contaminants and can alter the rates of mineral growth and dissolution processes (Hochella and White, 1990). Adsorption of impurities to kink sites on mineral surfaces can catalyze or inhibit dissolution (Ganor and Lasaga, 1998). For example, the rates of aluminosilicate weathering (Oelkers et al., 1994) and calcite precipitation (Meyer, 1984), two key reactions in the global C cycle, are affected by solution-borne impurities. The latter reaction is especially pertinent as more efficient ways of sequestering atmospheric C in geologic systems are sought in response to climate-change concerns (Lal and Kimble, 2000). In some minerals, the presence of specific impurities favors expression of different crystal faces and results in altered crystal morphologies (Li et al., 1990). Teng et al. (1998) report that the presence of organic impurities during growth dramatically changes surface energies and crystal morphologies; however, the mechanisms by which these impurities alter morphologies are not understood. Carbonate minerals are prevalent in soils, sediments, aquifers, and marine deposits and are known to adsorb and incorporate metallic cations of environmental and geochemical interest (Zachara et al., 1991). Calcite is the most common of the rhombohedral carbonate minerals and numerous studies have investigated the impact of trace-metal impurities on calcite crystal growth (Mucci and Morse, 1983; Meyer, 1984; Pingitore and Eastman, 1986; Pingitore et al., 1988; Dove and Hochella, 1993; Katz et al., 1993; Paquette and Reeder, 1990, 1995; Staudt et al., 1994; Reeder, 1996; Böttcher, 1998; Temmam et al., 2000). Fewer studies have investigated the impact of impurities on calcite crystal dissolution.

Terjesen et al. (1961) studied the effects of many heavy metal cations on the macroscopic calcite dissolution rate and found that the effectiveness of the metallic impurity in reducing the dissolution rate depended on whether the solubility of the metal carbonate was less than or greater than the solubility of calcite. Metal cations, with carbonate solubilities less than calcite (e.g., Pb, Cd, Cu, Zn, and Mn), were the most effective inhibitors of calcite dissolution, and their effectiveness was inversely related to the solubility product of the corresponding carbonate. Size of the cationic radius, on the other hand, appeared to have little effect on the ability to inhibit dissolution. Pb and Ba, which preferentially incorporate into an orthorhombic lattice, exhibited widely varying degrees of inhibition, as did Cu and Mg, which have similar cationic radii and preferentially incorporate into a rhombohedral lattice. Blanchard and Baer (1992) analyzed the dissolution rate of cobalt and manganese evaporated *in vacuo* onto the $(10\bar{1}4)$ surface of calcite. Manganese and cobalt treated surfaces were examined by x-ray photoelectron spectroscopy (XPS) before and after submersion in water. The rate of disappearance of manganese from the surface was two times slower than the rate of disappearance of cobalt, suggesting a greater interaction between manganese and calcite than between cobalt and calcite. Gutjahr et al. (1996) studied the effects of several divalent cations on growth and dissolution of calcite and noted that transition-metal cations that formed rhombohedral carbonates were more effective inhibitors than alkaline-earth cations that formed orthorhombic carbonates. They interpreted their kinetic results by assuming reversible adsorption of the cations to kink sites by using the Langmuir–Volmer model. These and other calcite dissolution studies that give rise to experimental rate equations (Plummer et al., 1978; Sjöberg, 1976; Chou et al., 1989; Svensson and Dreybrodt, 1992; Brown et al., 1993) produce information on a

* Author to whom correspondence should be addressed (Scott.Lea@pnl.gov).

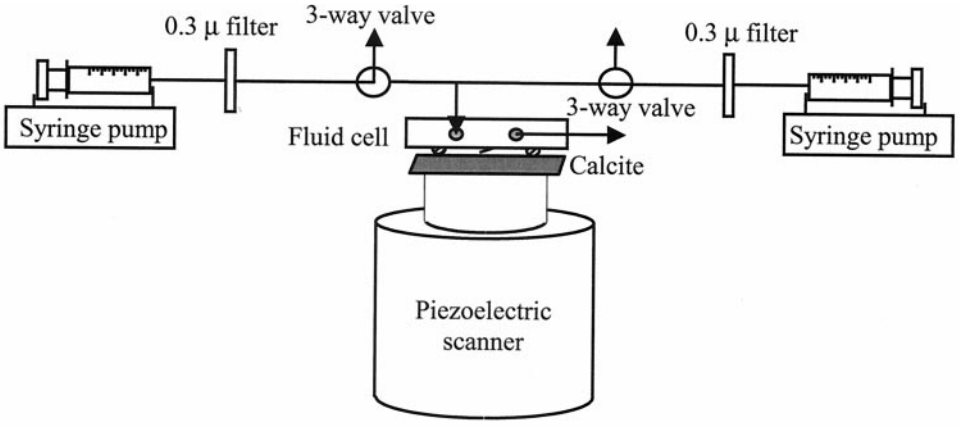

Fig. 1. Experimental setup for AFM studies of calcite dissolution.

macroscopic level only. The surface processes that govern these macroscopic observations generally are unknown.

Atomic force microscopy (AFM) techniques have proved useful over the past decade for elucidating atomic scale kinetics for in situ mineral dissolution (Gratz et al., 1991, 1993; Hillner et al., 1992a,b; Dove and Hochella, 1993; Liang et al., 1995, 1996a,b; Park et al., 1996a,b; Britt and Hlady, 1997). In this paper, we present an AFM study of impurity (Mn^{2+} and Sr^{2+}) interactions with monatomic steps on the ($10\bar{1}4$) calcite surface during dissolution. We also investigated the effect of CO_3^{2-} concentration on the dissolution process. Of the dissolution studies listed above, only those by Liang and Hillner measured step-edge migration rates, and neither of these groups rigidly controlled CO_3^{2-} levels in their dissolution experiments.

Our results are presented in terms of chemical properties of the bulk solution and the terrace-ledge-kink (TLK) model of the step edge. We used this model in our previous calcite dissolution work (Liang et al., 1996a,b; McCoy and LaFemina, 1997) to explain pit geometry and step-edge migration velocities in terms of double-kink formation and single-kink retreat rates. This model also has been successfully applied to the growth work of Teng et al. (1998).

2. MATERIALS AND METHODS

Calcium carbonate for AFM studies was Icelandic spar (Commercial Crystal Laboratories Inc., Naples, FL, USA) that was cleaved with a clean razor blade along the ($10\bar{1}4$) plane minutes before performing the experiments. The water used for solutions had a resistivity $\geq$ 18 MΩ/cm, and total organic C content of 3 ppb or less. NaOH, NaCl, $MnCl_2$, and $SrCl_2$ were reagent grade chemicals. Compressed synthetic air [pCO_2 = 3.64e-4 (CO_3^{2-} and Mn^{2+} experiments), 3.50e-4 (Sr^{2+} experiment)] initially was filtered and allowed to pass through two sequential water traps before bubbling through the NaOH solutions. Compressed CO_2 (commercial pure grade, pCO_2 = 0.998) from a gas cylinder was used without further treatment.

Experiments were performed at room temperature (nominally 22°C) with solutions at pH 8.8–8.9, a regime in which dissolution is dominated by the reaction (Chou et al., 1989; Plummer et al., 1978):

$$CaCO_3(s) \rightarrow Ca^{2+} + CO_3^{2-} \quad (1)$$

By specifying solution alkalinity (Stumm and Morgan, 1996) and then sparging the alkaline solution with air of known pCO_2, solution pH and the total amount of inorganic C dissolved in solution (C_T) were controlled. Concentrations of CO_3^{2-} and HCO_3^- species were calculated from solution alkalinity, pH, and appropriate equilibrium constants (Stumm and Morgan, 1996).

Three influent CO_3^{2-} concentrations were used: 150 μ**M**, 900 μ**M**, and a nominally CO_3^{2-}-free solution ($<$1 μ**M**). At pH 8.8–8.9, the C speciation in these solutions was dominated by HCO_3^- and the corresponding C_T concentrations were 4.3 **mM**, 18.5 **mM**, and $<$30 μ**M**, respectively. The 150 μ**M** CO_3^{2-} solutions were prepared by sparging a small amount of CO_2(g) through 4.4 **mM** NaOH solutions, so that the measured pH was close to its equilibrium pH, and then sparging synthetic air through the solution until the pH stabilized at its equilibrium value (i.e., 8.82). To obtain solutions with 900 μ**M** CO_3^{2-}, 19.5 **mM** NaOH solutions were sparged with CO_2(g) until the pH was well below 9. Upon sparging with synthetic air, the solution pH increased towards its equilibrium value of 9.3. Sparging was stopped when the pH reached 8.9. The $<$1 μ**M** CO_3^{2-} solution was prepared by adding aliquots of 0.01 **M** NaOH to water until the pH reached 8.9. For experiments with Mn^{2+} and Sr^{2+}, small aliquots of 1.0 **mM** $MnCl_2$ or 1.0 **mM** $SrCl_2$ were added to adjust the Mn^{2+} or Sr^{2+} concentration in the CO_3^{2-} solution. Control solutions containing NaCl also were prepared in order to observe any effect of Na^+ and Cl^- on dissolution. All solutions were prepared in high-density polyethylene bottles to avoid possible reaction with silica and used immediately after preparation.

The AFM was a NanoScope III (Digital Instruments, Santa Barbara, CA, USA) equipped with a fluid cell. Solutions were introduced into the cell using two syringe pumps and vinyl tubing with three-way valves attached (Fig. 1). Dead space in the tubing between the valves and the cell was minimal (120 μL). Nylon syringe filters (0.3 μm pore size) were used to dampen pump noise and to remove particulates. The calcite surface was imaged while the solution was flowing at a rate of 150 μL/min. This flow rate was previously determined to favor surface-reaction control of the kinetics for $<$1 μ**M** CO_3^{2-} solutions (Liang et al., 1995) and subsequently verified for 150 μ**M** CO_3^{2-} solutions in the absence of impurities. Because absolute step-velocity measurements are sensitive to sample drift, we used the ratio of slopes of deep-pit edges in conjunction with pit-opening velocity or summed-step velocity, V_{ss} (Liang et al., 1996b), to help determine the absolute velocities of individual steps.

All measurements were repeated several times to minimize apparent variations in absolute rates among different samples. Working at well-controlled CO_3^{2-} concentrations helped to minimize variations; however, at times variations were large enough to produce significant scatter in data obtained from many samples. In general, data provided in figures are representative of one experiment performed with one sample. Collectively, these data accurately represent trends observed in several different runs. Also worth mentioning is that reproducible data are most readily obtained on "high quality" crystals. Colton (1999) found reproducible results difficult to obtain when crystal quality varied significantly.

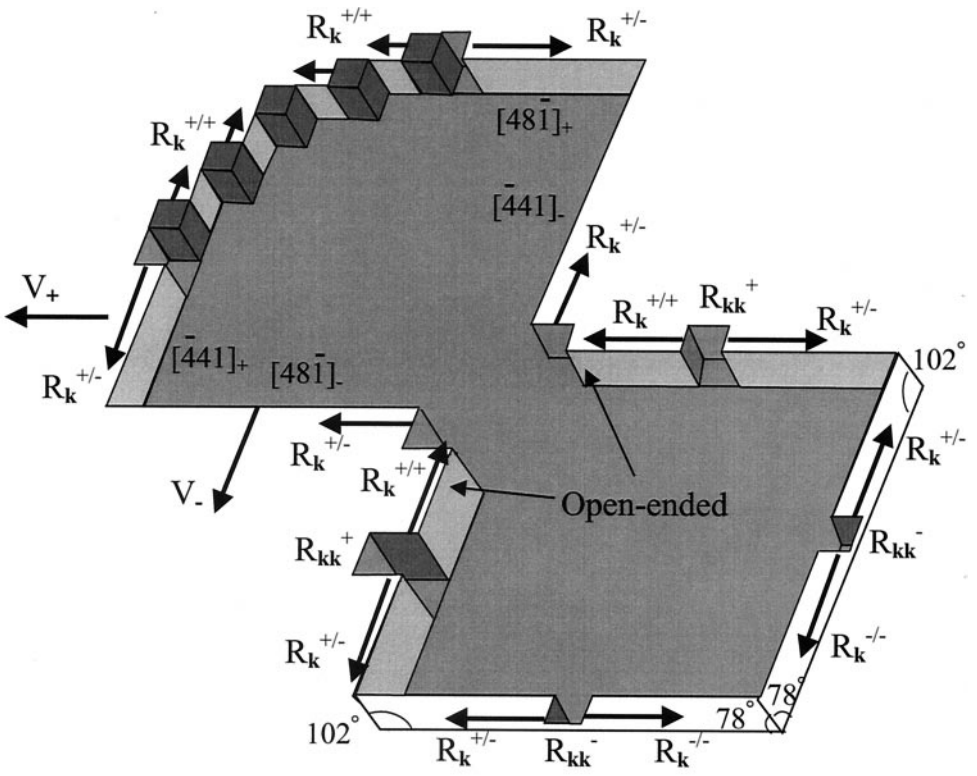

Fig. 2. Highly simplified schematic of two intersecting rhombohedral etch pits developed on the $(10\bar{1}4)$ surface of calcite.

3. RESULTS

As in previous work (Liang et al., 1995), dissolution occurred initially by formation of randomly spaced, shallow pits on the $(10\bar{1}4)$ surface. These shallow pits grew in size as dissolution proceeded until they annihilated each other. In addition to shallow pits, some deeper pits formed at defect sites. The slopes of deep-pit sides provide useful information about relative step velocities (Liang and Baer, 1997).

A few general observations about pit growth and step velocity from earlier work provide a context for understanding the measurements in this paper. For each pit, two of the step edges, which are on opposite sides of the pit, are aligned along the $<48\bar{1}>$ direction and the other two are aligned along the $<\bar{4}41>$ direction (Fig. 2). The steps are also designated "+" if the angle between the bottom of the pit and the step edge is 102° and "−" if the angle is 78°. The $[\bar{4}41]_+$ and $[48\bar{1}]_+$ steps are symmetrically related as are the $[\bar{4}41]_-$ and $[48\bar{1}]_-$ steps. The steps pointing to the interior of the intersecting pits are designated open-ended because they are confined at one end only. These steps migrate more rapidly than steps confined at both ends. Impurities, indicated by the dark cubes, preferentially adsorb to +/+ single-kink sites in the upper left-hand corner thereby slowing down their rate of retreat ($R_k^{+/+}$) and causing rounding of the corner.

For shallow pits large enough to be readily measured, receding step-edge velocities are constant regardless of pit size, and velocity magnitudes are morphologically specific. The less confined, obtuse $[48\bar{1}]_+$ and $[\bar{4}41]_+$ edges move at identical velocities (V_+) and, in solutions far below saturation, are faster than the more confined, acute $[48\bar{1}]_-$ and $[\bar{4}41]_-$ edges, which also move at identical velocities (V_-). Previously measured velocities in solutions far from saturation ranged from 2.9 nm/s to 3.4 nm/s for V_+ and 1.3 nm/s to 1.5 nm/s for V_- (Liang et al., 1996b). Hillner et al. (1992b) measured 3.5 nm/s for V_+. Because circumstances exist where "slow" acute steps migrate faster than "fast" obtuse steps, we will abandon the "fast" and "slow" designation adopted by Liang et al. (1995) and strictly refer to steps as + or − following Staudt et al. (1994).

3.1. Effect of CO_3^{2-}

Step-edge migration velocities decreased with increased $[CO_3^{2-}]$. The extent of this decrease was step dependent—that is, an increase in $[CO_3^{2-}]$ had a greater effect on the obtuse $[48\bar{1}]_+$ and $[\bar{4}41]_+$ steps than on the acute $[48\bar{1}]_-$ and $[\bar{4}41]_-$ steps. This was most evident in the slopes of deep-pit sides, which are inversely proportional to step velocities. At <1 μ**M** CO_3^{2-} (Fig. 3a), the slopes of the $[48\bar{1}]_+$ and $[\bar{4}41]_+$ edges in the deep pits were less than the slopes of the $[48\bar{1}]_-$ and $[\bar{4}41]_-$ edges, indicating faster step velocities for the $[48\bar{1}]_+$ and $[\bar{4}41]_+$ steps. At 150 μ**M** CO_3^{2-} (Fig. 3b), the slopes were nearly equal indicating similar step velocities. At 900 μ**M** CO_3^{2-} (Fig. 3c), however, $[48\bar{1}]_-$ and $[\bar{4}41]_-$ steps were moving at velocities greater than the $[48\bar{1}]_+$ and $[\bar{4}41]_+$ steps.

Increasing $[CO_3^{2-}]$ affected both deep- and shallow-pit shape. At very low $[CO_3^{2-}]$, the pit shape was rhombohedral (Fig. 3a), reflecting the rhombohedral symmetry of the calcite crystal and the preferred planes of dissolution. However, as the

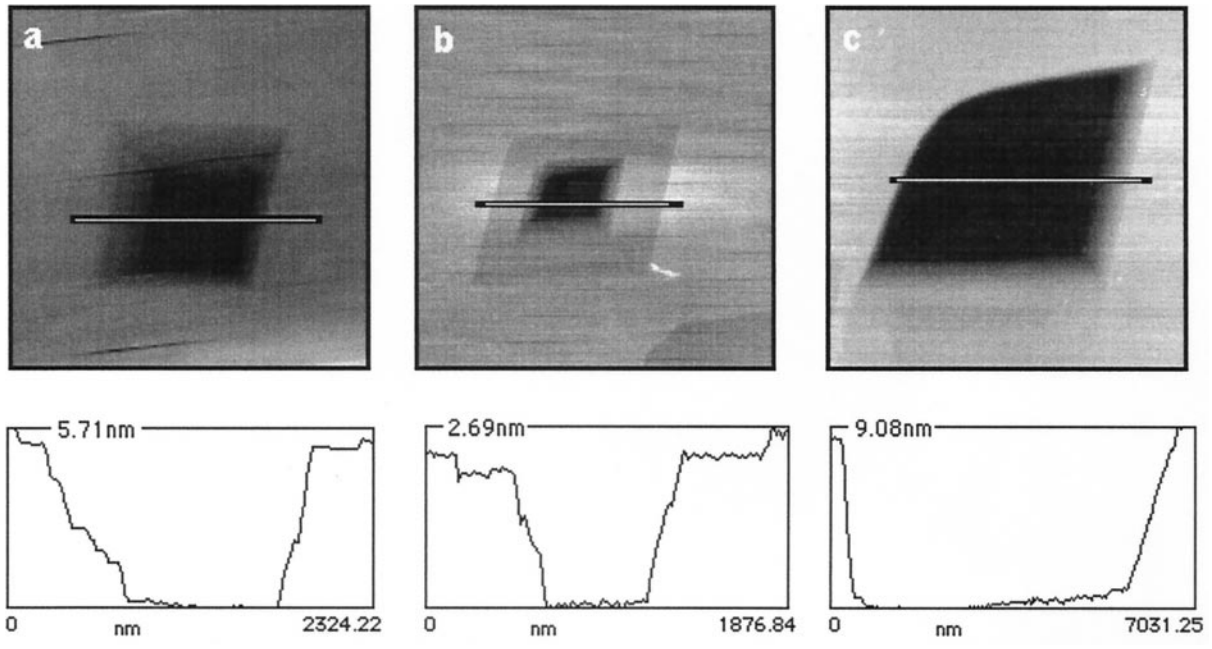

Fig. 3. Topographic AFM images (top) and cross sections (bottom) of deep pits formed during the dissolution of calcite at pH 8.9 in solutions containing different $[CO_3^{2-}]$. The $[\bar{4}41]_+$ and $[48\bar{1}]_+$ steps are on the left and top, respectively, of each pit. a) < 1 **μM** $[CO_3^{2-}]$, 4.85 $\times$ 4.85 μm; b) 150 **μM** $[CO_3^{2-}]$, 5.00 $\times$ 5.00 μm; and c) 900 **μM** $[CO_3^{2-}]$, 10.00 $\times$ 10.00 μm.

$[CO_3^{2-}]$ increased, the pit corner between the $[48\bar{1}]_+$ and $[\bar{4}41]_+$ step edges became rounded (Fig. 3b). The corner between the $[48\bar{1}]_-$ and $[\bar{4}41]_-$ step edges remained sharp despite the decreased velocity of the $[48\bar{1}]_-$ and $[\bar{4}41]_-$ step edges. Increasing the $[CO_3^{2-}]$ further led to more rounding between the $[48\bar{1}]_+$ and $[\bar{4}41]_+$ step edges, but to no detectable rounding between the $[48\bar{1}]_-$ and $[\bar{4}41]_-$ step edges (Fig. 3c). Switching back to the <1 **μM** CO_3^{2-} solution resulted in etch pits resuming rhombohedral dissolution.

As a control, step-edge migration velocities were measured by using <1 **μM** CO_3^{2-} solutions at pH 8.9 with 20 **mM** NaCl added. The velocities were identical to those measured in the absence of NaCl and the shallow pits remained rhombohedral at a $[Na^+]$ equal to that in the 900 **μM** CO_3^{2-} solutions (data not shown). This experiment verified that CO_3^{2-} (or HCO_3^-), rather than Na^+ or Cl^-, caused the decreased step-edge velocity and rounded corner observed between the $[48\bar{1}]_+$ and $[\bar{4}41]_+$ step edges.

Summed step-edge migration velocities (V_{ss}) for the three CO_3^{2-} levels were determined by measuring shallow-pit widths as a function of time. As the $[CO_3^{2-}]$ increased from <1 **μM**, V_{ss} decreased from 4.0 nm/s to 1.6 nm/s at 150 **μM** CO_3^{2-} and to 0.73 nm/s at 900 **μM** CO_3^{2-} (Fig. 4, Table 1). The migration rates of the individual $[\bar{4}41]_+$ and $[\bar{4}41]_-$ steps were also determined from the V_{ss} and slope ratios as a function of $[CO_3^{2-}]$. The much stronger effect of CO_3^{2-} on the $[\bar{4}41]_+$ (and, by symmetry, $[48\bar{1}]_+$) steps is seen clearly in Fig. 4 and by changes in slope ratio (Table 1).

3.2. Effect of Mn^{2+}

The effect of $[Mn^{2+}]$ on step-edge migration velocities was observed using a series of $MnCl_2$ solutions prepared in 150 **μM** CO_3^{2-}. The smallest $[Mn^{2+}]$ used in these experiments was 0.1 **μM**, which was equivalent to a $MnCO_3$ saturation ratio in the bulk solution (Ω_{MnCO_3}) of 0.07 calculated by MINTEQA2. These calculations used the K_{sp} and ion-pair association constants of Nordstrom et al. (1990) for the $Mn/CO_3^{2-}/HCO_3^-$ system, with the exception that log K = 4.32 was used for formation of the $MnCO_3^o$(aq) ion pair (Langmuir, 1979). As noted by Sternbeck (1997), the value given by Nordstrom et al. (1990) (log K = 4.90) is likely too high. The highest $[Mn^{2+}]$

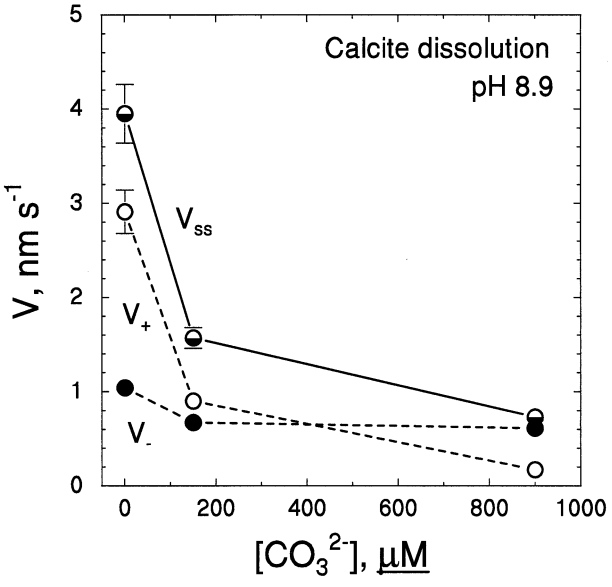

Fig. 4. Effect of $[CO_3^{2-}]$ on step-edge migration velocities of shallow pits during calcite dissolution at pH 8.9.

Table 1. Experimental parameters, etch-pit slope ratios, and step-edge migration velocities measured in calcite-dissolution experiments.

Added ion[a]	Conc. **μM**	Nominal Ω_{MeCO_3}	V_{ss} nm/s	n (V_{ss} pits)	+/− Slope ratio	V_+ nm/s	V_- nm/s
CO_3^{2-}	<1	ND[b]	3.95 ± 0.31 (1.00)[c]	8	0.36	2.91 ± 0.23 (1.00)[c]	1.04 ± 0.08 (1.00)[c]
	150	[0.07][d]	1.57 ± 0.11 (0.40)	6	0.75	0.90 ± 0.06 (0.31)	0.67 ± 0.05 (0.64)
	900	ND	0.73 ± 0.04 (0.18)	5	3.7	0.17 ± 0.01 (0.06)	0.61 ± 0.03 (0.59)
Mn^{2+}	0	[0.07][d]	1.57 ± 0.11 (1.00)	6	0.75	0.90 ± 0.06 (1.00)	0.67 ± 0.05 (1.00)
	0.1	0.07	1.56 (0.99)	1	0.75	0.89 (0.99)	0.67 (1.00)
	0.5	0.34	1.53 ± 0.06 (0.97)	6	0.75	0.87 ± 0.03 (0.97)	0.66 ± 0.03 (0.99)
	1.0	0.68	0.69 ± 0.05 (0.44)	10	0.75	0.39 ± 0.03 (0.43)	0.30 ± 0.02 (0.45)
	2.0	1.4 [0.08][d]	0.13 ± 0.01 (0.08)	6	0.85	0.07 ± 0.01 (0.08)	0.06 ± 0.01 (0.09)
Sr^{2+}	0	[0.07][d]	1.89 ± 0.21 (1.00)	18	0.85	1.03 ± 0.11 (1.00)	0.86 ± 0.10 (1.00)
	2.25	0.33	1.85 ± 0.23 (0.98)	26	0.85	1.00 ± 0.12 (0.97)	0.85 ± 0.11 (0.99)
	4.5	0.66	1.49 ± 0.18 (0.79)	18	ND	ND	ND
	7.5	1.1	1.54 ± 0.17 (0.81)	18	ND	ND	ND
	12	1.8	1.34 ± 0.10 (0.71)	16	3.62	0.29 ± 0.02 (0.28)	1.05 ± 0.08 (1.22)
	24	3.5	1.15 ± 0.11 (0.61)	22	7.21	0.14 ± 0.01 (0.14)	1.01 ± 0.10 (1.17)

[a] Mn^{2+} and Sr^{2+} added in 150 **μM** CO_3^{2-} solution.
[b] ND = not determined.
[c] Numbers in parentheses represent the step velocity normalized to the step velocity obtained for the lowest concentration of additive.
[d] Numbers in brackets are $\boldsymbol{\Omega_{calcite}}$, based on analysis of AFM cell effluent.

used in our experiments was 2 **μM**, which corresponded to a Ω_{MnCO_3} of 1.4 in the bulk solution. Upon contact of this solution with calcite, the Ω_{MnCO_3} near the calcite surface would be expected to increase due to the release of $[CO_3^{2-}]$ as calcite dissolved.

At $[Mn^{2+}]$ less than 0.5 **μM**, there was no effect of Mn^{2+} on the dissolution rate (Fig. 5). However, as the $[Mn^{2+}]$ exceeded 0.5 **μM** ($\Omega_{MnCO_3} = 0.13$), V_{ss} decreased. At 2 **μM** Mn^{2+}, V_{ss} was more than an order of magnitude smaller than at 0.5 **μM** Mn^{2+}. This phenomenon stems from competing reactions—calcite dissolves because the solution is undersaturated with respect to calcite, while Mn^{2+} undergoes a significant sorption/precipitation reaction as Ω_{MnCO_3} approaches unity.

Although V_{ss} decreased significantly as $[Mn^{2+}]$ increased, the ratio of V_+ to V_-, which is the inverse of the slope ratio, remained essentially unchanged (Table 1). This result suggests that Mn^{2+} interacts with both step edges to a similar extent.

In addition to the step velocity changes, we observed nucleation and growth of a Mn-rich phase during calcite dissolution at the highest $[Mn^{2+}]$. This phase appeared to grow in specific directions relative to the substrate and stopped when it intersected a single atomic level step on the calcite surface. These observations will be discussed in a later paper.

3.2. Effect of Sr^{2+}

The effect of Sr^{2+} on step-edge migration velocities was observed by using 150 **μM** CO_3^{2-} solutions spiked with $SrCl_2$ to concentrations that ranged from 2.25 to 24 **μM** Sr. By using the K_{sp} and ion-pair association constants for the $Sr/CO_3^{2-}/HCO_3^-$ system recommended by Nordstrom et al. (1990), the

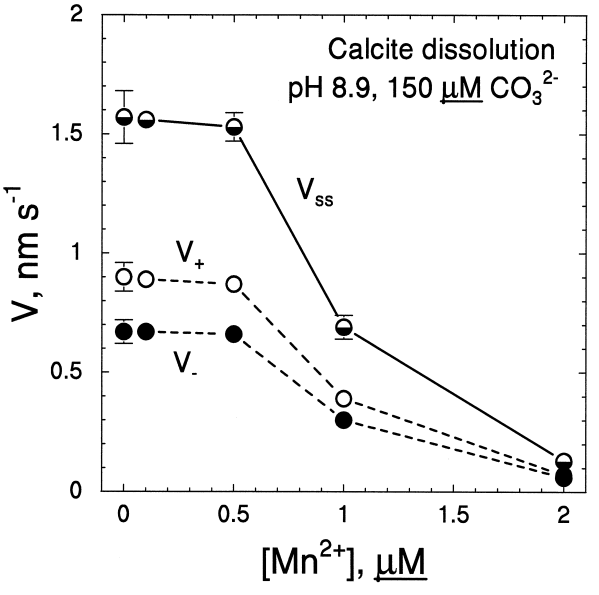

Fig. 5. Effect of $[Mn^{2+}]$ on step-edge migration velocities of shallow pits during calcite dissolution in 150 **μM** $[CO_3^{2-}]$ solutions at pH 8.9.

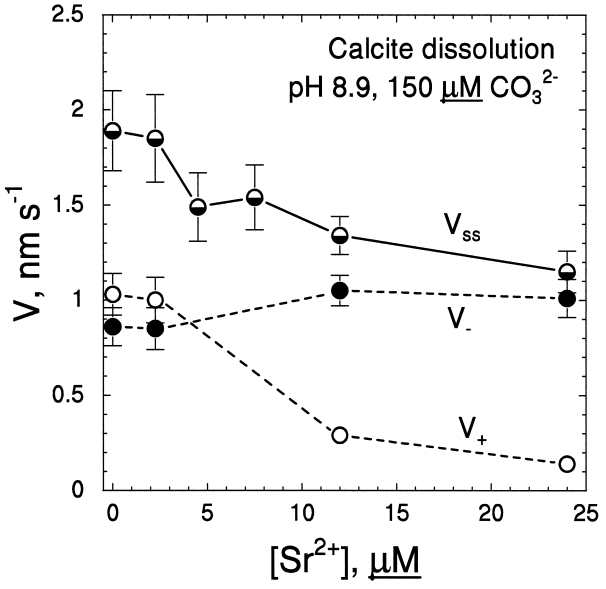

Fig. 6. Effect of $[Sr^{2+}]$ on step-edge migration velocities of shallow pits during calcite dissolution in 150 μ**M** $[CO_3^{2-}]$ solutions at pH 8.9.

corresponding range in Ω_{SrCO_3} values calculated for these solutions was 0.33 to 3.5. Thus, several of the influent solutions were supersaturated with respect to $SrCO_3$(s). At $[Sr^{2+}]$ of 2.5 μ**M** ($\Omega_{SrCO_3} = 0.33$), no significant effect on calcite dissolution rate (V_{ss}) was observed (Fig. 6). At higher $[Sr^{2+}]$, V_{ss} decreased steadily. At 24 μ**M** ($\Omega_{SrCO_3} = 3.5$), V_{ss} was about 60% of the rate when no Sr^{2+} was added. All of the decrease in V_{ss} came as a result of decreases in V_+ (Fig. 6, Table 1). In fact, values for V_- actually increased at higher $[Sr^{2+}]$. The etch pits also developed rounded corners between the sterically open $[\bar{4}41]_+$ and $[48\bar{1}]_+$ steps that were similar in appearance to the rounded corner shown in Fig. 3c for high $[CO_3^{2-}]$.

These results indicate that Sr^{2+} interacts primarily with the sterically open sites on the surface of calcite during dissolution and that, like the situation for Mn^{2+}, competition between the precipitation/adsorption of $SrCO_3$ and the dissolution of $CaCO_3$ is occurring at these sites.

4. DISCUSSION

4.1. Calcite Reaction Rates

A mechanistic expression for the net rate of calcite reaction, **R**, which is equal to the dissolution rate, $\mathbf{R_{for}}$, minus the growth rate, $\mathbf{R_{back}}$, was developed by Plummer et al. (1978) and modified slightly by Chou et al. (1989). These researchers considered three possible surface reactions, of which only one (given in Eqn. 1) is important under the chemical regime of our experiments (pH $\sim$ 9, $P_{CO_2} \ll 0.1$ atm). Based on this reaction, $\mathbf{R_{for}}$ is constant and the changes in the apparent dissolution rate observed in our experiments must stem from changes in $\mathbf{R_{back}}$. For the calcite/water system at constant temperature and pH and in the absence of impurities, $\mathbf{R_{back}}$ is predicted to be directly proportional to the ion-activity product of Ca^{2+} and CO_3^{2-} (Chou et al., 1989). Thus,

$$\mathbf{R} = k_{for} - k_{back}\, \mathbf{a}_{Ca^{2+}}\, \mathbf{a}_{CO_3^{2-}} \quad (2)$$

wherein an inverse linear dependence of calcite reaction rate on the saturation ratio of the solution with respect to calcite, $\mathbf{\Omega_{Calcite}}$, is seen. As noted by Plummer et al. (1978), however, this approach does not account for the effects of "foreign ions" known to inhibit the calcite reaction.

The step-edge migration velocity results we obtained showed independent behavior of the two types of steps with respect to changes in the solution composition. The obtuse $[\bar{4}41]_+$ and $[48\bar{1}]_+$ steps were consistently the most sensitive to the solution composition, whereas sensitivity of the acute $[\bar{4}41]_-$ and $[48\bar{1}]_-$ steps varied with the ion. For example, with Sr^{2+}, no effect was seen on the acute $[\bar{4}41]_-$ and $[48\bar{1}]_-$ steps, whereas with Mn^{2+} changes in concentration affected both types of steps equally. Perhaps the greatest surprise was the much stronger effect of CO_3^{2-} on the migration rates of the obtuse step edges, even though it is a structural ion in both types of steps. Similar anisotropic effects have been seen in calcite growth studies (Paquette and Reeder, 1995; Staudt et al., 1994; Reeder, 1996) where the fastest moving step edges in undoped calcite crystals were reported to be the structurally open $[\bar{4}41]_+$ and $[48\bar{1}]_+$ steps. Paquette and Reeder (1995) reasoned that Ca^{2+} preferentially incorporated into the structurally open $[\bar{4}41]_+$ and $[48\bar{1}]_+$ steps. This anisotropy during growth is consistent with our observations of increased back reaction at the $[\bar{4}41]_+$ and $[48\bar{1}]_+$ steps as the levels of CO_3^{2-} increase from about 1 to 900 μ**M**.

Although the decreases seen in step-edge migration velocities are inversely correlated with increases in added-ion concentration, the dependence is not the simple linear dependence that is predicted by Eqn. 2. Rather our results suggest two distinct regions where step-edge velocities are affected by added-ion concentration. The first region occurs at low added-ion concentration where a slight, possibly linear, decrease in step-edge velocity occurs as the added-ion concentration increases. Upon reaching a threshold impurity concentration, a second region is observed where the decrease in step-edge velocity changes to a strong nonlinear dependence on the added-ion concentration. Although the linear relationship in Eqn. 2 would not necessarily be expected for the experiments with Mn^{2+} and Sr^{2+}, it certainly would be expected for the variable-CO_3^{2-} experiments where a near-constant $\mathbf{a_{Ca^{2+}}}$ could be assumed. Similar experiments conducted in our laboratory at constant $[CO_3^{2-}]$ and variable $[Ca^{2+}]$ (Colton, 1999), also showed step-edge migration velocities to be nonlinear with respect to $\mathbf{a_{Ca^{2+}}}$ and $\mathbf{\Omega_{Calcite}}$. The flow regime in our experiments was at the lower limit of the region where surface control of the reaction rate was operable far from saturation (Liang and Baer, 1997). Dissolution experiments conducted on the same crystal surface with a range of flow rates (130–570 μL/min) and in the absence of impurities yielded step-edge migration velocities identical to those observed at 150 μL/min (i.e., $V_{ss} = 1.59 \pm 0.19$, $n = 31$). Thus, it seems unlikely that a mixture of surface and diffusion control could have yielded the nonlinearity observed.

General mathematical models of the effects of impurities on mineral growth and dissolution processes also suggest that a simple linear relationship is unlikely. Gutjahr et al. (1996) fit their calcite dissolution data to an expression in which the

relative rate was proportional to $1/(1 + k[Me])$, where k is a constant and [Me] the solution concentration of the impurity metal cation.

Ganor and Lasaga (1998) constructed mineral-dissolution models that assume the rapid adsorption of inhibitors and catalysts onto a mineral surface followed by a slow hydrolysis step. Their models included both independent adsorption and competitive adsorption of inhibiting and catalytic species on surface sites. Both types of models predict a region at low inhibitor concentration where essentially no effect on dissolution is seen followed by a second region at higher inhibitor concentration where a significant effect is seen. The independent-adsorption model, which yielded better fits in the three noncarbonate examples they tested, predicts only a limited region of inhibitor concentration (perhaps a 10× range) where linear dissolution would occur under a constant catalyst concentration. A similar situation seems to apply to our experiments where wider ranges in inhibiting-ion concentration (≥10×) were explored under otherwise constant conditions.

Davey and Mullin (1974) incorporated adsorption into a TLK growth model in which the step-edge velocity depended on the fractional coverage of the surface by the impurity, θ. Kubota and Mullin (1995) modified this model by adding an "effectiveness" parameter, α, to correct θ for differences in the numbers of sorption sites for impurity and structural molecules and for the size, shape, and orientation of the sorbed impurity. Kubota and Mullin (1995) used the modified model to fit several noncarbonate experimental data sets. Linear inhibition of growth occurred only when $\alpha \gg 1$ (i.e., the surface density of impurity-sorption sites was much lower than that of kink sites). For values of $\alpha = 1$, where impurity sorption sites and kink sites have comparable surface densities, log-linear inhibition of growth was seen, similar to that inhibition we observed in the second region above the threshold concentration of added ion. However, no threshold value for the impurity effect was predicted with this TLK model.

Other TLK models of impurity effects have been developed (Sears, 1958; Cabrera and Vermilyea, 1958) but do not explicitly consider the threshold values for initiation of the effect. Sears (1958) noted that "the rate of step motion should be insensitive to poison concentration in solution corresponding to less than monostep coverage." Although this could be taken as a thermodynamic statement, we note that during dissolution there is a step lifetime and no effect would be expected when the sorption of impurities at steps is slow in comparison to the step lifetime.

4.2. Site-Specific TLK Model

The above models consider adsorption effects in a general way and assume "static" sorption equilibrium. Because impurities could block specific types of sites and those sites are easily identified on the $(10\bar{1}4)$ calcite surface, it seemed reasonable and desirable to develop a simple site-specific TLK model to help interpret the step-edge migration velocity data. The model is framed in terms of the dynamic arrival rate of impurity species at the calcite surface relative to the rates at which new double-kink sites are generated and single-kink sites annihilated. Many simplifying assumptions are used to facilitate analysis and they will be examined more fully in a separate paper. We assume initially that the impurity species, which we will denote as **M**, perturbs the normal reactions that occur at a step by 'blocking' the reactions at specific sites. The impurity is assumed to adsorb at any point on the surface and to diffuse rapidly on the surface to specific sites where blocking occurs.

By using the TLK framework of Liang and Baer (1997), dissolution of a smooth step first occurs by creation of double-kink sites, followed by lateral movement of single-kinks toward pit corners. The back reaction, or growth, occurs by adding species at single-kink sites. While "+/−" single-kink sites exist on each of the four steps of an etch pit, the "−/−" single-kink sites reside entirely on $[\bar{4}41]_-$ and $[48\bar{1}]_-$ edges and the "+/+" single-kink sites reside entirely on $[\bar{4}41]_+$ and $[48\bar{1}]_+$ edges. Because the "+/+" single-kinks are unique to the step edges most affected by changes in CO_3^{2-} concentration (the edges that round), we hypothesize that the back reaction occurs preferentially at "+/+" single-kink sites. McCoy et al. (unpublished data) added back-reaction rates to their previously developed kinetic Monte Carlo model for calcite (McCoy and LaFemina, 1997). By significantly increasing the rate of back reaction at "+/+" sites, they not only demonstrated considerable slowing of $[\bar{4}41]_+$ and $[48\bar{1}]_+$ steps, but also were able to produce pits with the rounded corner between these steps as observed in Fig. 3b and c.

If we assume both single-kink sites on a step behave identically (i.e., the isotropic model of Burton et al., 1951), step retreat is initiated by nucleation of a double-kink site (a kink-antikink pair) along a step edge, followed by lateral motion of each single-kink towards the corners of the pit. Once a step reaches a critical minimum length, the steady-state step velocity expressed in terms of double-kink formation and single-kink retreat is:

$$\mathbf{V_o} = \mathbf{a}[\mathbf{R_{kk}}(2\mathbf{R_k})]^{1/2} \tag{3}$$

where $\mathbf{R_{kk}}$ is the rate of double-kink nucleation at a single site on a step, and $\mathbf{R_k}$ is the rate at which a single-kink retreats one lattice unit, **a**.

Consider **L** to be the average distance between double-kink nucleation sites along a step. The number of lattice sites between double-kink nucleation sites along a step is then given by $\mathbf{n} = \mathbf{L}/\mathbf{a}$. The average lifetime of a single-kink is:

$$\boldsymbol{\tau}_\mathbf{k} = \mathbf{n}/2\mathbf{R_k} \tag{4a}$$

and the average time required to nucleate a double-kink is:

$$\boldsymbol{\tau}_{\mathbf{kk}} = 1/\mathbf{n}\mathbf{R_{kk}}. \tag{4b}$$

Because at steady state $\boldsymbol{\tau}_\mathbf{k} = \boldsymbol{\tau}_{\mathbf{kk}}$, we can express $\mathbf{R_k}$ in terms of $\mathbf{R_{kk}}$, as:

$$\mathbf{R_k} = (\mathbf{n}^2/2)\mathbf{R_{kk}} \tag{4c}$$

When **M** is present, Eqn. 3 may be written as:

$$\mathbf{V_{(M)}} = \mathbf{a}[\mathbf{R'_{kk}}(2\mathbf{R'_k})]^{1/2} \tag{5}$$

where $\mathbf{R'_{kk}}$ and $\mathbf{R'_k}$, respectively, represent $\mathbf{R_{kk}}$ and $\mathbf{R_k}$ in the presence of **M**. The ratio of the velocities (Eqns. 3 and 5) is given by:

$$\mathbf{V_{(M)}}/\mathbf{V_o} = [\mathbf{R'_{kk}}\mathbf{R'_k}/\mathbf{R_{kk}}\ \mathbf{R_k}]^{1/2} \tag{6}$$

We now consider how **M** influences $\mathbf{R_{kk}}$ and $\mathbf{R_k}$. The following simple derivation ignores several aspects of statistical distribution. For this model, we assume that 1) **M** affects $\mathbf{R_{kk}}$ and $\mathbf{R_k}$ only when it is actually adsorbed to ('blocking') the step site, and 2) most **M** species adsorbed at a step readily diffuse along the step and eventually attach to a kink site. We also assume that if **M** occupies a single-kink site or if a kink-kink nucleation site has **M** adsorbed to it, the reaction rate at that site is zero. We define $\mathbf{R_M}$ as the rate of **M** adsorption at a single step site, assuming the site is not already occupied by **M**, and note that it depends on the solution activity of **M**. As the actual dependence is unknown, we write the general kinetic rate-law expression as:

$$\mathbf{R_M} = \mathbf{k}\,(\mathbf{a_M})^{\mathbf{r}}, \tag{7}$$

where **r** is a fitting factor. The average time for **M** to adsorb per step length is:

$$\boldsymbol{\tau}_{\mathbf{M(n)}} = \mathbf{a}/(\mathbf{L}\mathbf{R_M}) = 1/(\mathbf{n}\mathbf{R_M}) \tag{8a}$$

Because there are two single-kink sites per step length, the average time for **M** to adsorb and block each single-kink site is:

$$\boldsymbol{\tau}_{\mathbf{M(n/2)}} = 2\boldsymbol{\tau}_{\mathbf{M(n)}} = 2/(\mathbf{n}\mathbf{R_M}). \tag{8b}$$

When the time for **M** to adsorb $\boldsymbol{\tau}_{\mathbf{M(n/2)}}$ (Eqn. 8b), is longer than the single-kink lifetime $\boldsymbol{\tau}_{\mathbf{k}}$, there is little chance of **M** sorption and migration to a single-kink site. As a result:

$$\mathbf{R'_k} \approx \mathbf{R_k}. \tag{9a}$$

$$\boldsymbol{\tau}_{\mathbf{M(n/2)}} \geq \boldsymbol{\tau}_{\mathbf{k}}$$

As the time required for **M** to adsorb, diffuse, and block a single-kink site decreases, the average single-kink retreat rate also decreases. By using $\boldsymbol{\tau}_{\mathbf{M(n/2)}}/\boldsymbol{\tau}_{\mathbf{k}}$ to represent the fraction of a single-kink lifetime that remains unaffected by **M** sorption, the steady-state rate of single-kink retreat in the presence of **M** may be approximated by:

$$\mathbf{R'_k} \approx [\boldsymbol{\tau}_{\mathbf{M(n/2)}}/\boldsymbol{\tau}_{\mathbf{k}}]\mathbf{R_k}. \tag{9b}$$

$$\boldsymbol{\tau}_{\mathbf{M(n/2)}}/\boldsymbol{\tau}_{\mathbf{k}}$$

Substituting from Eqns. 4a and 8b yields:

$$\mathbf{R'_k} \approx [2/\mathbf{n}\mathbf{R_M})][2\mathbf{R_k}/\mathbf{n}]\mathbf{R_k}. \tag{9c}$$

$$\boldsymbol{\tau}_{\mathbf{M(n/2)}} \leq \boldsymbol{\tau}_{\mathbf{k}}$$

Further substituting from Eqn. 4c and rearranging, we obtain:

$$\mathbf{R'_k}/\mathbf{R_k} \approx 2\mathbf{R_{kk}}/\mathbf{R_M}. \tag{9d}$$

$$\boldsymbol{\tau}_{\mathbf{M(n/2)}} \leq \boldsymbol{\tau}_{\mathbf{k}}$$

The influence of **M** on the rate of double-kink formation $\mathbf{R_{kk}}$ also must be considered. We assume that the formation of a double-kink is not possible at a site where **M** is present. Therefore, the impact of M on $\mathbf{R_{kk}}$ depends on the number of **M** adsorbed along the step of length **L**. By using the ratio of the average step lifetime $\boldsymbol{\tau}_{\mathbf{k}}$ to the time of **M** sorption for the entire step $\boldsymbol{\tau}_{\mathbf{M(n)}}$ (Eqn. 8a), the number of sites that remain unblocked along the step may be expressed as $\mathbf{n} - [\boldsymbol{\tau}_{\mathbf{k}}/\boldsymbol{\tau}_{\mathbf{M(n)}}]$, and the fraction of unblocked sites as $1 - (1/\mathbf{n})[\boldsymbol{\tau}_{\mathbf{k}}/\boldsymbol{\tau}_{\mathbf{M(n)}}]$. Thus the steady-state rate of double-kink formation in the presence of **M** may be approximated by:

$$\mathbf{R'_{kk}} \approx \mathbf{R_{kk}}[1 - (1/\mathbf{n})(\boldsymbol{\tau}_{\mathbf{k}}/\boldsymbol{\tau}_{\mathbf{M(n)}})] \tag{10a}$$

Substituting and rearranging as before, we obtain:

$$\mathbf{R'_{kk}}/\mathbf{R_{kk}} \approx [1 - \mathbf{R_M}/(\mathbf{n}\mathbf{R_{kk}})] \tag{10b}$$

Eqns. 7, 9a, 9d, and 10b can now be substituted into Eqn. 6 to provide expressions as a function of $\mathbf{a_M}$:

$$\mathbf{V_{(M)}}/\mathbf{V_o} \approx [1 - (\mathbf{k}/\mathbf{R_{kk}})(\mathbf{a_M})^{\mathbf{r}}(1/\mathbf{n})]^{1/2} \tag{11a}$$

$$\boldsymbol{\tau}_{\mathbf{M(n/2)}} \geq \boldsymbol{\tau}_{\mathbf{k}}$$

$$\mathbf{V_{(M)}}/\mathbf{V_o} \approx [2(\mathbf{R_{kk}}/\mathbf{k})(1/\mathbf{a}_{\mathrm{M}})^{\mathbf{r}} - (2/\mathbf{n})]^{1/2} \tag{11b}$$

$$\boldsymbol{\tau}_{\mathbf{M(n/2)}} \leq \boldsymbol{\tau}_{\mathbf{k}}$$

Thus, the site-specific TLK site-blocking model describes one region where step-migration velocity is controlled solely by the impact of **M** on the rate of double-kink formation (Eqn. 11a), and a second region at higher $\mathbf{a_M}$ where the impact of **M** on single-kink retreat rates dominates (Eqn. 11b).

As an initial test of the model concept, we assumed that the Mn^{2+}(aq) species is the form of the impurity, **M**. By using MINTEQA2 to calculate the $\mathbf{a_{Mn^{2+}}}$ from influent concentration values, an excellent fit to the V_{ss} data is obtained when **r** is set equal to 2 (Fig. 7a). For this fit, $\mathbf{n} = 36$, and $\mathbf{R_{kk}}/\mathbf{k} = 7.4\mathrm{e}-15$. If $\mathbf{r} = 1$, as would be expected if a linear kinetic model (e.g., Eqn. 2) were operable, a poorer fit is obtained and a shorter step length is predicted ($\mathbf{n} = 8$, $\mathbf{R_{kk}}/\mathbf{k} = 6.4\mathrm{e}\text{-}8$), although the same general features are seen (Fig. 7a). We do not have a rigorous mechanistic interpretation of the apparent second-order dependence on $\mathbf{a_{Mn^{2+}}}$, nor is such warranted given the large number of assumptions used to derive this simple model. However, we note that with **r** set to 2, the model also provides an excellent fit to V_{ss} data collected by Colton (1999) for different levels of Ca^{2+} in the absence of impurities (Fig. 7b, $\mathbf{n} = 55$, $\mathbf{R_{kk}}/\mathbf{k} = 9.0\mathrm{e}\text{-}12$).

For Sr^{2+}(aq), the situation is more complicated given the anisotropic dissolution that occurred and the probable precipitation of strontianite [$SrCO_3$(s)] at $[Sr^{2+}] \geq 7.5\ \mu$M. Unlike the situation with Mn, no evidence for epitaxial precipitates was seen in the Sr AFM data. The current version of the TLK model could not account for the increase in V_- that was observed at higher $[Sr^{2+}]$. Intuitively, this increase can be explained in terms of no sorption of Sr^{2+} ions at the sterically hindered "$-/-$" kink sites, and the occurrence of $SrCO_3$(s) precipitation, which would consume CO_3^{2-} ions near the surface and thus lower the $\boldsymbol{\Omega}_{\mathbf{Calcite}}$. Application of the model to the sparse V_+ data for Sr^{2+} yields an acceptable fit when **r** is set to 1, $\mathbf{n} = 25$, and $\mathbf{R_{kk}}/\mathbf{k} = 7.5\mathrm{e}\text{-}7$ (Fig. 7b). Because the MINTEQA2 calculations were based in influent concentrations rather than actual measurements of effluent values, however, the values of $\mathbf{a_{Sr^{2+}}}$ used in the model are likely higher than the actual values and the results skewed to lower **r**.

The current data focus on Mn and Sr adsorption while the calcite substrate is dissolving. Paquette and Reeder (1995), by using x-ray fluorescence, also found the larger Sr^{2+} cation (131 pm) to be preferentially incorporated during growth at the more

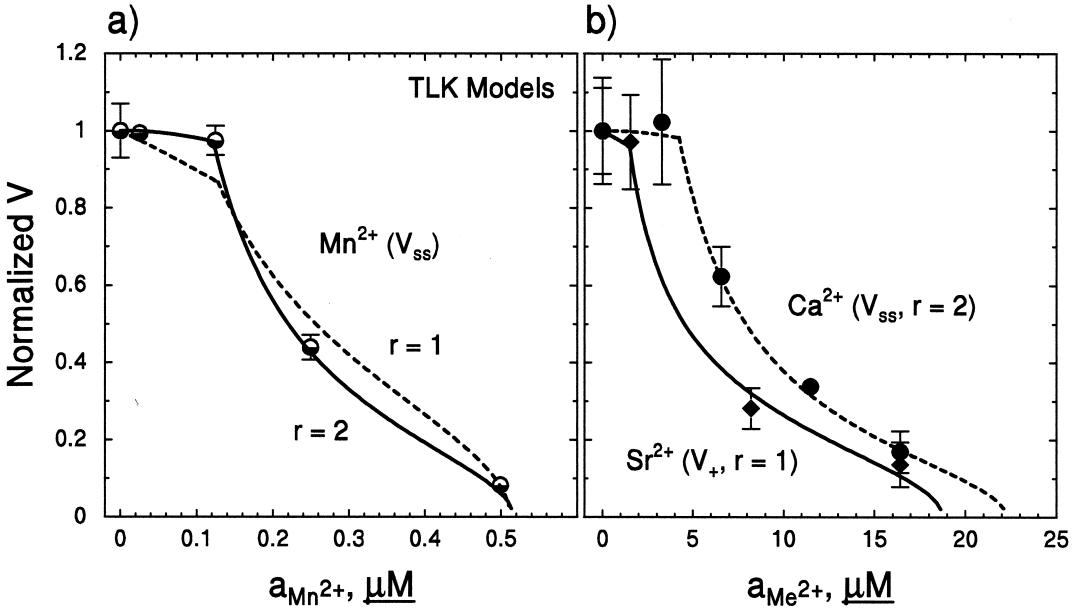

Fig. 7. Fits of the TLK model to normalized step-edge migration velocity data by using metal-ion activities for a) Mn^{2+}, and b) Sr^{2+} and Ca^{2+}.

structurally open $[\bar{4}41]_+$ steps. This is similar to our dissolution results. Additionally, they reported the smaller Mn^{2+} cation (83 pm) is preferentially incorporated at the more structurally confined $[\bar{4}41]_-$ steps. This differs from our measurements where both $[\bar{4}41]_+$ steps and $[\bar{4}41]_-$ steps are influenced by the presence of Mn^{2+}. Paquette and Reeder initially concluded that the distribution of cationic impurities at the different steps depended on cationic size; however, a later study (Reeder, 1996) using zinc cations suggested size is not the sole determining factor in distribution. Specific interactions between the divalent cation and the surface sites or the presence of ligands may also play a significant role. Further work by Hemming et al. (1998), albeit on anion incorporation, also suggests size is not the sole limiting determinant in distribution.

We also note that there are significant differences between the growth processes observed by Paquette and Reeder (1995) and the solution conditions of the current study. In growth conditions, the solution may or may not be oversaturated with respect to the impurity carbonate (i.e., rhodochrosite or strontianite), but is well oversaturated with respect to calcite. Additionally, the impurity cations must first sorb to the surface and then be incorporated into the "bulk" of the crystal. In the current study, the solution is well undersaturated with respect to calcite, but oversaturated with respect to the impurity carbonate. For these conditions, we assume that the impurity cation influences calcite dissolution by sorbing at single-kink sites thereby slowing calcite dissolution by blocking a specific single-kink site. Because single-kink sites normally dissolve faster than the rate that double-kink sites form (dissolution along a straight part of a step), dissolution is slowed. If this occurs at only one type of single-kink site (e.g., +/+), pits can become rounded. If this occurs relatively uniformly, pit shape will not change.

4.3. Ion Pairs

In deriving the TLK model, the actual nature of the structural growth units and the inhibiting units, **M**, were not specified. The initial application of the model assumed the divalent cations as the active species because these were the factors being manipulated. Eventually a neutral $CaCO_3$ unit must form for the crystal to grow. The difficulty is in assessing whether this unit forms in place on the surface (i.e., sequential addition of cation and anion to a kink site) or whether it forms at or near the surface and then attaches to the kink site.

As the rate-limiting step in calcite precipitation is believed to be the dehydration of the cation, several authors have speculated that partly dehydrated neutral or cationic ion pairs that form in solution are the actual growth units. Our study of impurity effects on the back-reaction rate of calcite affords a unique opportunity to examine the possible role of ion-pair formation in that we can manipulate the total concentration of metal-carbonate ion pairs independently of the $\mathbf{\Omega_{Calcite}}$. If the ion pairs are the growth units, rather than individual ions, and if the ion pairs have similar affinities for a kink site, then the onset of the inhibition of dissolution should occur at a single ion-pair activity. That is, at the step-edge migration velocity breakpoint [$\boldsymbol{\tau_{M(n/2)} = \tau_k}$], the sum of the $\mathbf{a_{CaCO3^\circ}}$ and $\mathbf{a_{MnCO3^\circ}}$ in the Ca:Mn system should be equal to the sum of $\mathbf{a_{CaCO3^\circ}}$ and $\mathbf{a_{SrCO3^\circ}}$ in the Ca:Sr system and to the $\mathbf{a_{CaCO3^\circ}}$ in a pure Ca system. The possible formation of precipitates at the higher concentrations of Mn and Sr has little effect on the breakpoint location, thus eliminating this source of uncertainty in the analysis.

To test this hypothesis, the values for $\mathbf{a_{CaCO3^\circ}}$, $\mathbf{a_{MnCO3^\circ}}$, and $\mathbf{a_{SrCO3^\circ}}$ calculated from influent concentration data by using MINTEQA2 were summed as appropriate for the system and plotted vs. normalized values of V_+ (Fig. 8a). The obtuse step

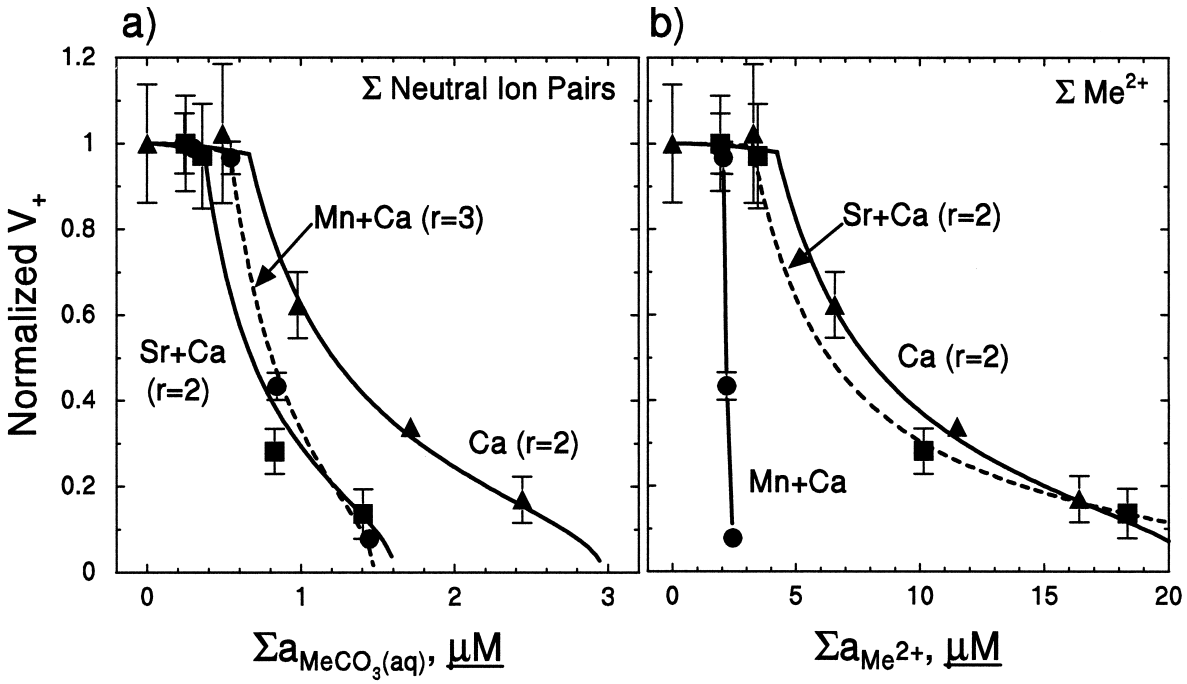

Fig. 8. Fits of the TLK model to normalized V_+ data using sums of a) neutral ion-pair ($MeCO_3^o$) activities, and b) metal cation (Me^{2+}) activities.

was selected because all three cations are known to react with this step. As can be clearly seen, the step-edge migration velocity breakpoints for the three systems coincided at a summed ion-pair concentration of about 0.53 ± 0.14 μ**M**. A similar approach, in which summed cation activities were plotted, yielded coincidence at 3.3 ± 1.1 μ**M** (Fig. 8b). A comparison of the relative errors for the two systems (27% for the summed ion pairs, 34% for the summed cations) shows little difference. Use of the Nordstrom et al. (1990) value for formation of the $MnCO_3^o$(aq) ion-pair changes the relative errors only slightly (to 31% and 35% for ion pairs and cations, respectively). We do note, however, that the TLK model could not be fit satisfactorily to the summed Mn^{2+} + Ca^{2+} data, whereas all the summed ion-pair data were easily fit with similar values for **n**. Assuming that our TLK model accurately portrays the interactions at the surface and that both impurity and structural species contribute to the step-edge migration velocities, the ability to describe the changes in velocities when summed ion-pair data are used lends credence to the hypothesis that neutral ion pairs formed in solution are the primary growth units. Clearly, a larger data set that includes experiments with other metal ions is needed to confirm this observation.

5. CONCLUSIONS

The dissolution rate and etch-pit morphology are highly dependent on the presence of cationic impurities and CO_3^{2-} ions in solution. While we cannot directly determine the exact mechanisms or species involved, we argue that the changes in dissolution rate and etch-pit morphology are kinetically driven by the arrival rates of ions or ion pairs at the calcite surface. Kink propagation is retarded by adsorption of the ions or ion pairs along steps and at single-kink sites.

Although there are many assumptions and approximations in the model, the essence is that the adsorbing species can both influence the formation of double-kink sites and block (or at least inhibit) the dissolution of single-kink sites. At low concentrations, retardation of double-kink formation is the dominant process. At higher concentrations, retardation of single-kink dissolution along the step is dominant. A sharp change in step-edge migration velocities is predicted at the threshold concentration where rate control shifts from double-kink formation to single-kink dissolution. This change is clearly seen in our AFM data suggesting that the TLK blocking model is qualitatively correct.

Before general application of the model can be made, however, further development and refinement will be needed. This effort, now underway in our laboratory, includes the collection of coupled AFM and solution-chemical data for other impurities, and the development of more detailed knowledge of binding at steps and single-kinks and diffusion along terraces to step edges. Efforts to adapt a kinetic Monte Carlo model (similar to that used for pure dissolution) to this process are also underway.

Acknowledgments—This work was supported by the Division of Geosciences, Office of Basic Energy Science, U.S. Department of Energy. PNNL is a multiprogram national laboratory operated for the Department of Energy by Battelle Memorial Institute under contract DE-AC06-76RL01830.

The authors thank Mark Engelhard for XPS analyses, and John Daschbach for helpful discussions and careful examination of the blocking-model presentation.

REFERENCES

Blanchard D. L. Jr. and Baer D. R. (1992) The interactions of Co, Mn and water with calcite surfaces. *Surf. Sci.* **276,** 27–39.

Böttcher M. E. (1998) Manganese(II) partitioning during experimental precipitation of rhodocrosite-calcite solid solutions from aqueous solution. *Mar. Chem.* **62,** 287–297.

Britt D. W. and Hlady V. (1997) In-situ atomic force microscope imaging of calcite etch pit morphology changes in undersaturated and 1-hydroxyethylidene-1,1-diphosphonic acid poisoned solutions. *Langmuir* **13,** 1873–1876.

Brown, C. A., Compton R. G., and Narramore C. A. (1993) The kinetics of calcite dissolution/precipitation. *J. Colloid Interface Sci.* **160,** 372–379.

Burton W. K., Cabrera N., and Frank F. C. (1951) The growth of crystals and equilibrium structure of their surfaces. *Phil. Trans. Roy. Soc. (London) A* **243**, 299–358.

Cabrera N. and Vermilyea D. A. (1958) The growth of crystals from solution. In *Growth and Perfection of Crystals* (eds. R. H. Doremus, B. W. Roberts, and D. Turnbull), pp. 393–408. Wiley.

Chou L., Garrels R. M., and Wollast R. (1989) Comparative study of the kinetics and mechanisms of dissolution of carbonate minerals. *Chem. Geol.* **78,** 269–282.

Colton N. G. (1999) *Solution Effects on Calcite Dissolution*. M.S. Thesis, Washington State Univ.

Davey R. J. and Mullin J. W. (1974) Growth of the {100} faces of ammonium dihydrogen phosphate crystals in the presence of impurities. *J. Crystal Growth* **26,** 45–51.

Dove P. M. and Hochella M. F. Jr. (1993) Calcite precipitation mechanisms and inhibition by orthophosphate: in situ observations by scanning force microscopy. *Geochim. Cosmochim. Acta* **57,** 705–714.

Ganor J. and Lasaga A. C. (1998) Simple mechanistic models for inhibition of a dissolution reaction. *Geochim. Cosmochim. Acta* **62,** 1295–1306.

Gutjahr A., Dabringhaus H., and Lacmann R. (1996) Studies of the growth and dissolution kinetics of the $CaCO_3$ polymorphs calcite and aragonite II. The influence of divalent cation additives on the growth and dissolution rates. *J. Cryst. Growth* **158,** 310–315.

Gratz A. J., Manne S., and Hansma P. K. (1991) Atomic force microscopy of atomic-scale ledges and etch pits formed during dissolution of quartz. *Science* **251,** 1343–1346.

Gratz A. J., Hillner P. E., and Hansma P. K. (1993) Step dynamics and spiral growth on calcite. *Geochim. Cosmochim. Acta* **57,** 491–495.

Hemming N. G., Reeder R. J., and Hart S. R. (1998) Growth-step-selective incorporation of boron on the calcite surface. *Geochim. Cosmochim. Acta* **62,** 2915–2922.

Hillner P. E., Manne S., Gratz A. J., and Hansma P. K. (1992a) AFM images of dissolution and growth on a calcite crystal. *Ultramicroscopy* **42–44**, 1387–1393.

Hillner P. E., Gratz A. J., Manne S., and Hansma P. K. (1992b) Atomic-scale imaging of calcite growth and dissolution in real time. *Geology* **20,** 359–362.

Hochella M. F. Jr. and White A. F. (1990) Mineral-water interface geochemistry: An overview. In *Mineral-Water Interface Geochemistry, Reviews in Mineralogy*, Vol. 23 (eds. M. F. Hochella Jr. and A. F. White), pp. 1–16. Mineral. Soc. Amer.

Katz J. L., Reick M. R., Herzog R. E., and Parsiegla K. I. (1993) Calcite growth inhibition by iron. *Langmuir* **9,** 1423–1430.

Kubota N. and Mullin J. W. (1995) A kinetic model for crystal growth from aqueous solution in the presence of impurity. *J. Cryst. Growth* **152,** 203–208.

Lal R. and Kimble J. M. (2000). Inorganic carbon and the global C cycle: Research and development priorities. In *Global Climate Change and Pedogenic Carbonates* (eds. R. Lal, J. M. Kimble, H. Eswaran, and B. A. Stewart), pp. 291–302. Lewis Publishers.

Langmuir D. (1979) Techniques of estimating thermodynamic properties for some aqueous complexes of geochemical interest. In *Chemical Modeling in Aqueous Systems, ACS Symposium Series*, Vol. 93 (ed. E. A. Jenne), pp. 353–388. Am. Chem. Soc.

Li L., Tsukamoto K., and Sunagawa K. I. (1990) Impurity adsorption and habit changes in aqueous solution grown KCl crystals. *J. Cryst. Growth* **99,** 150–155.

Liang Y., Lea A. S., and Baer D. R. (1995) Dissolution of $CaCO_3$ $(10\bar{1}4)$ surface. *Mat. Res. Soc. Symp. Proc.* **355,** 409–414.

Liang Y., Baer D. R., McCoy J. M., Amonette J. E., and LaFemina J. P. (1996a) Dissolution kinetics at the calcite-water interface. *Geochim. Cosmochim. Acta* **60,** 4883–4887.

Liang Y., Baer D. R., McCoy J. M., and LaFemina J. P. (1996b) Interplay between step velocity and morphology during the dissolution of $CaCO_3$ surface. *J. Vac. Sci. Technol. A* **14,** 1368–1375.

Liang Y. and Baer D. R. (1997) Anisotropic dissolution at the $CaCO_3$ $(10\bar{1}4)$–water interface. *Surf. Sci.* **373,** 275–287.

McCoy J. M. and LaFemina J. P. (1997) Kinetic Monte Carlo investigation of pit formation at the $CaCO_3$ $(10\bar{1}4)$ surface-water interface. *Surf. Sci.* **373,** 288–299.

Meyer H. J. (1984) The influence of impurities on the growth rate of calcite. *J. Crystal Growth* **66,** 639–646.

Mucci A. and Morse J. W. (1983) The incorporation of Mg^{2+} and Sr^{2+} into calcite overgrowths: Influences of growth rate and solution composition. *Geochim. Cosmochim. Acta* **47,** 217–233.

Nordstrom D. K., Plummer L. N., Langmuir D., Busenburg E., May H. M., Jones B. F., and Parkhurst D. L. (1990) Revised chemical equilibrium data from major mineral reactions and their limitations. In *Chemical Modeling of Aqueous Systems II, ACS Symposium Series*, Vol. 416 (ed. D. C. Melchior and R. L. Bassett), pp. 398–413. Am. Chem. Soc.

Oelkers E. H., Schott J., and Devidal J.-L. (1994) The effect of aluminum, pH, and chemical affinity on the rates of aluminosilicate dissolution reactions. *Geochim. Cosmochim. Acta* **58,** 2011–2024.

Paquette J. and Reeder R. J. (1990) New type of compositional zoning in calcite: Insights into crystal growth mechanisms. *Geology* **18,** 1244–1247.

Paquette J. and Reeder R. J. (1995) Relationship between surface structure, growth mechanism, and trace element incorporation in calcite. *Geochim. Cosmochim. Acta* **59,** 735–749.

Park N.-S., Kim M.-W., Langford S. C., and Dickinson J. T. (1996a) Tribological enhancement of $CaCO_3$ dissolution during scanning force microscopy. *Langmuir* **12,** 4599–4604.

Park N.-S., Kim M.-W., Langford S. C., and Dickinson J. T. (1996b) Atomic layer wear of single-crystal calcite in aqueous solution using scanning force microscopy. *J. Appl Phys.* **80,** 2680–2685.

Pingitore N. E. Jr. and Eastman M. P. (1986) The coprecipitation of Sr^{2+} with calcite at 25°C and 1 atm. *Geochim. Cosmochim. Acta* **50,** 2195–2203.

Pingitore N. E. Jr., Eastman M. P., Sandige M., Oden K., and Freiha B. (1988) The coprecipitation of manganese(II) with calcite: An experimental study. *Mar. Chem.* **25,** 107–120.

Plummer L. N., Wigley T. M. L., and Parkhurst D. L. (1978) The kinetics of calcite dissolution in CO_2-water systems at 5°C to 60°C and 0.0 to 1.0 atm CO_2. *Am. J. Sci.* **278,** 179–216.

Reeder R. J. (1996) Interaction of divalent cobalt, zinc, cadmium, and barium with the calcite surface during layer growth. *Geochim. Cosmochim. Acta* **60,** 1543–1552.

Sears G. W. (1958) The effect of poisons on crystal growth. In *Growth and Perfection of Crystals* (eds. R. H. Doremus, B. W. Roberts, and D. Turnbull), pp. 441–445. Wiley.

Sjoberg E. L. (1976) A fundamental equation for calcite dissolution kinetics. *Geochim. Cosmochim. Acta* **40,** 441–447.

Staudt W. J., Reeder R. J., and Schoonen M. A. A. (1994) Surface structural controls on compositional zoning of SO_4^{2-} and SeO_4^{2-} in synthetic calcite single crystals. *Geochim. Cosmochim. Acta* **58,** 2087–2098.

Sternbeck J. (1997) Kinetics of rhodochrosite crystal growth at 25°C: The role of surface speciation. *Geochim. Cosmochim. Acta* **61,** 785–793.

Stumm W. and Morgan J. J. (1996) *Aquatic Chemistry: An Introduction Emphasizing Chemical Equilibria in Natural Waters, 3rd ed*. Wiley.

Svensson U. and Dreybrodt W. (1992) Dissolution kinetics of natural calcite minerals in CO_2-water systems approaching calcite equilibrium. *Chem. Geol* **100,** 129–145.

Temmam M., Paquette J., and Vali H. (2000) Mn and Zn incorporation into calcite as a function of chloride aqueous concentration. *Geochim. Cosmochim. Acta* **64,** 2417–2430.

Teng H. H., Dove P. M., Orme C. A. and De Yoreo J. J. (1998) Thermodynamics of calcite growth: Baseline for understanding biomineral formation. *Science* **282,** 724–727.

Terjesen S. G., Erga O., Thorsen G., and Ve A. (1961) Phase boundary processes as rate determining steps in reactions between solids and liquids. *Chem. Eng. Sci.* **74,** 277–288.

Zachara J. M., Cowan C. E., and Resch C. T. (1991) Sorption of divalent metals on calcite. *Geochim. Cosmochim. Acta* **55,** 1549–1562.